Photodissociation dynamics of ClN$_3$ at 193 nm

Scott J. Goncher, Niels E. Sveum, David T. Moore,
Nate D. Bartlett, and Daniel M. Neumark[a]
Department of Chemistry, University of California, Berkeley, California 94720
and Chemical Sciences Division, Lawrence Berkeley National Laboratory, Berkeley, California 94720

Photofragment translational spectroscopy was used to identify the primary and secondary reaction pathways in 193 nm photodissociation of chlorine azide (ClN$_3$) under collision-free conditions. Both the molecular elimination (NCl+N$_2$) and the radical bond rupture channel (Cl+N$_3$) were investigated and compared with earlier results at 248 nm. The radical channel strongly dominates, just as at 248 nm. At 193 nm, the ClN$_3$ ($\widetilde{C}\,^1A''$) state is excited, rather than the $\widetilde{B}\,^1A'$ state that is accessed at 248 nm, resulting in different photofragment angular distributions. The chlorine translational energy distribution probing the dynamics of the radical bond rupture channel shows three distinct peaks, with the two fastest peaks occurring at the same translational energies as the two peaks seen at 248 nm that were previously assigned to linear and "high energy" N$_3$. Hence, nearly all the additional photon energy relative to 248 nm appears as N$_3$ internal excitation rather than as translational energy, resulting in considerably more spontaneous dissociation of N$_3$ to N$_2$+N. © *2006 American Institute of Physics.* [DOI: 10.1063/1.2400854]

I. INTRODUCTION

The photodissociation dynamics of the ClN$_3$ molecule have attracted considerable recent interest. Primary photodissociation of ClN$_3$ can occur via molecular elimination

$$ClN_3 + h\nu \rightarrow NCl + N_2 \tag{1}$$

or through radical bond rupture

$$ClN_3 + h\nu \rightarrow Cl + N_3. \tag{2}$$

The energetics at 0 K for all possible photodissociation products are shown in Fig. 1.[1,2] Channel (1) is of interest because metastable NCl ($\alpha\,^1\Delta$) has been successfully used to achieve the population inversion of iodine atoms necessary for lasing in an all gas phase chemical iodine laser (AGIL),[3] and ClN$_3$ photolysis has been considered as a possible source of this species. Recent work by Hansen and Wodtke at photolysis wavelengths around 240 nm has suggested that channel (2) produces not only linear N$_3$ as a product, but also a higher energy cyclic N$_3$ isomer,[4] a result consistent with recent work in our group at 248 nm.[5] The work reported here focuses on the photodissociation dynamics of ClN$_3$ using 193 nm light in order to obtain new insights into the two channels and to compare the results to those obtained at lower photon energies.

The ClN$_3$ molecule has three unstructured absorption bands in the ultraviolet centered at 350, 250, and 205 nm.[6,7] Several groups[7–10] have investigated the production of channel (1) from excitation of the two higher energy bands, which have been assigned to the $\widetilde{B}\,^1A'$ and $\widetilde{C}\,^1A''$ states.[11] Much of this work has focused on characterization of the three NCl states accessible by photolysis at these wave-lengths (see Fig. 1), with the underlying assumption that channel (1) was, in fact, the major primary photoproduct.

The possible significance of channel (2) became apparent only after velocity map ion imaging (VMI) experiments performed by Hansen and Wodtke,[4] in which Cl atoms produced by photolysis near 235 nm were ionized and imaged. The Cl fragment showed a markedly bimodal translational energy distribution in this work and in more recent VMI experiments performed over a wider wavelength range.[12] The faster Cl products were attributed to production of linear N$_3$ with relatively little internal energy. The slower peak suggested production of a higher energy form of the N$_3$ molecule. The energetics of this peak were, in fact, consistent with the production of cyclic N$_3$, a high energy, metastable form of N$_3$ whose existence had been predicted in electronic structure calculations.[13] The experimental VMI results have prompted additional theoretical studies of the properties of cyclic N$_3$ by Morokuma and co-workers.[2,14] These predict that the cyclic structure lies 30.3 kcal/mol above the linear isomer and has a 33.1 kcal/mol barrier for dissociation to N$_2$(X)+N(^2D) products.

The original VMI experiments on ClN$_3$ motivated a collaborative effort between our laboratory and Hansen and Wodtke, in which photofragment translational spectroscopy (PTS) was used to study ClN$_3$ photodissociation at 248 nm.[5,15] In this experiment, scattered photoproducts were ionized by electron impact and mass selected, and their translational energy and angular distributions were determined. PTS allows one to investigate channels (1) and (2) with approximately equal sensitivity, and to permit a more detailed investigation of channel (2) via detection of both the Cl and momentum-matched N$_3$ photofragments. This work showed that the branching ratio between the molecular elimination (1) and radical bond rupture (2) channels is
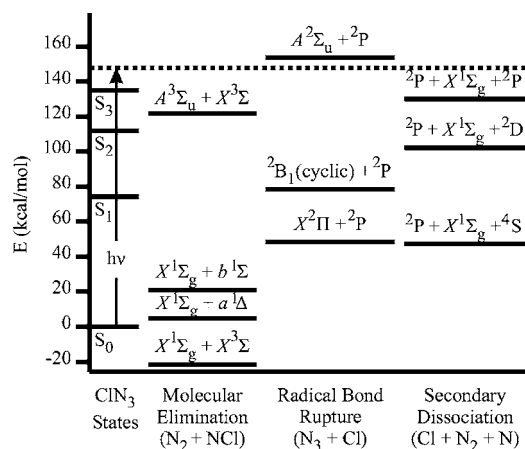
FIG. 1. Energy level diagram for the possible decomposition pathways of ClN_3 referenced to its ground state. Each energy level shows the final electronic states of the fragments of each channel. The arrow shows the levels accessed by a 193 nm photon.

$NCl+N_2/Cl+N_3=0.05\pm0.03/0.95\pm0.03$, in notable contrast with earlier results which pointed to $NCl(a\ ^1\Delta)+N_2$ as the dominant dissociation channel.[7,9,10,16] This discrepancy most likely reflects the formation of $NCl+N_2$ from secondary $Cl+N_3$ reactions in the earlier experiments.

In the PTS experiments, the Cl fragments exhibited a bimodal translational energy distribution experimentally indistinguishable to that found in the earlier imaging study. A bimodal distribution of N_3 products was also observed, providing the first unambiguous evidence that two distinct populations of N_3 are formed in ClN_3 photolysis. The faster Cl and N_3 peaks were momentum matched, i.e., fitted with the same center-of-mass translational energy distribution. This distribution was consistent with prior assignment of this faster channel to linear N_3 production. However, the slower (HEF, for high energy form) N_3 peak was considerably depleted relative to the slower Cl peak, particularly at the lowest translational energies. This result indicates that the slowest N_3 fragments were produced with sufficient internal energy to undergo spontaneous dissociation to N_2+N on a time scale faster than detection. Both the energetics and depletion of the HEF-N_3 were consistent with predictions for metastable, cyclic N_3, as is very recent work in which the photoionization thresholds were measured for both forms of N_3 produced from ClN_3 photodissociation at 248 nm.[17]

In this paper, we describe PTS experiments on 193 nm photodissociation of ClN_3. These experiments were motivated in part to check if the branching ratio for channels (1) and (2) changed at the higher photon energy, but also to determine the robustness of the two N_3 populations and their dynamical origins. The higher energy photon used for dissociation now probes the $\tilde{C}\ ^1A''$ state of the parent molecule, resulting in photofragment angular distributions characteristic of a perpendicular transition. Radical bond rupture results in a translational energy distribution for the Cl atom comprising three peaks, two of which have translational energies nearly identical to the $Cl+N_3$(linear) and $Cl+N_3$(HEF) products from 248 nm photolysis. Hence, it appears that the additional photon energy relative to 248 nm is channeled primarily into product internal excitation, an unusual result for such a small molecule. This extra internal energy results in substantial secondary dissociation of the N_3 fragment. Molecular elimination is found to still be a very minor channel, with a branching ratio between reactions (1) and (2) of $NCl+N_2/Cl+N_3=0.4\pm0.2/99.6\pm0.2$; the translational energy release for this channel is also comparable to that seen at 248 nm.

II. EXPERIMENT

The molecular-beam photodissociation instrument on which these experiments were performed has been described in detail previously.[18,19] A mixture of 10% Cl_2 seeded in He or Ne was passed over moist sodium azide (NaN_3) suspended in glass wool in order to prepare the ClN_3 used in these experiments. Excess water was removed by passing the mixture through a drying agent (Drierite). Under normal operating conditions, mass spectral analysis of the beam showed NCl^+, an ionizer-induced fragment of ClN_3^+, and little or no Cl_2^+. When Cl_2^+ signal could be detected, the NaN_3 sample was replaced.

Using a backing pressure of ~0.5 bar, a pulsed molecular beam was formed by expanding the ClN_3 mixture into vacuum through a piezoelectrically actuated pulsed valve.[20] The velocity distribution of the parent ClN_3 molecular beam was characterized by using a retractable slotted chopper wheel to modulate the molecular beam. After passing through two collimating skimmers, the molecular beam intersected a 28 ns pulsed beam of 193 nm laser light produced by a Lambda Physik ArF excimer laser. When measurements of the photodissociation anisotropy were taken, laser light was polarized by placing a stack of eight quartz Brewster angle plates in the light path. This polarizer removed all light except light polarized at 90° or 0° with respect to the plane defined by the molecular beam and the propagation direction of light. Otherwise, light was unpolarized. The laser and value were operated at 100 and 200 Hz, respectively, to allow for background subtraction of the parent molecular beam. The laser output (~70 mJ energy/pulse) was focused to an ~10 mm^2 spot at the region of intersection with the molecular beam.

Photofragments scattered in the plane of the molecular laser beam were detected as a function of laboratory scattering angle, Θ, using a rotatable, triply differentially pumped mass spectrometer. After passing through three collimating apertures, the photofragments were ionized by electron impact, mass selected with a quadrupole mass filter, and detected with a Daly-style detector.[18] Ionized photoproducts were counted as a function of time using a multichannel scaler interfaced to a computer, yielding a photofragment time-of-flight (TOF) distribution for a specific mass-to-charge ratio (m/e). In these experiments, photoproducts with $m/e=49(NCl^+)$, $42(N_3^+)$, $35(Cl^+)$, $28(N_2^+)$, and $14(N^+)$ were measured, producing TOF distributions of all possible photofragments in ClN_3 dissociation. TOF distributions were analyzed using forward-convolution programs designed to simulate TOF spectra based on the center-of-mass translational energy distribution of the photofragments.
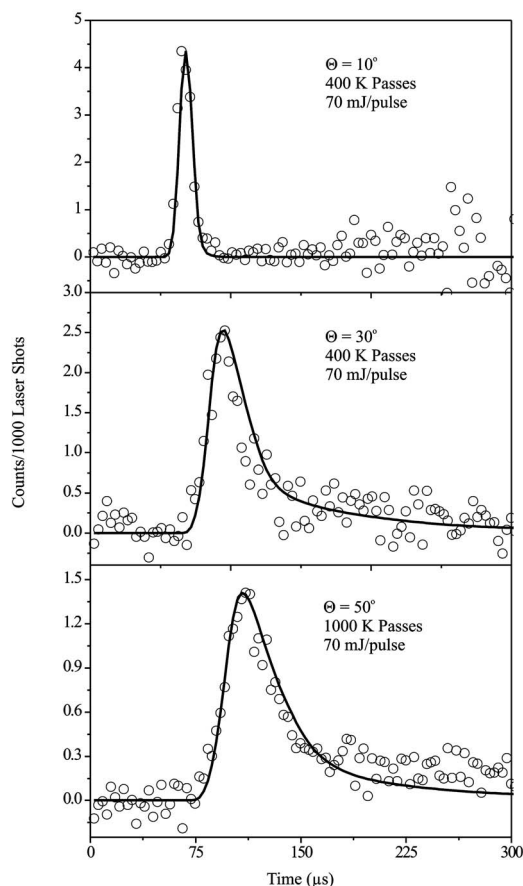
FIG. 2. TOF spectra of $m/e=49(\text{NCl}^+)$ at detection angles $\Theta=10°$, $30°$, and $50°$ taken with the parent molecular beam seeded in Ne. For all spectra, the open circles represent the data and the solid line represents the forward-convolution fit to the data using the $P(E_T)$ distribution shown in Fig. 8.

III. RESULTS

Figure 2 shows TOF spectra of the NCl fragments ($m/e=49$) produced from channel (1) at various scattering angles Θ. Figure 3 shows TOF spectra for the Cl fragments ($m/e=35$) and the N_3 fragments ($m/e=42$) produced from channel (2). In all TOF spectra, open circles represent the data and the various lines show the results of the forward-convolution simulations of the experiment obtained from center-of-mass translational energy distributions (see Sec. IV). These spectra were taken with the laser unpolarized and the parent molecular beam seeded in Ne. Each $m/e=49$ spectrum comprises a single peak, while the $m/e=35$ spectra all show at least three distinct peaks. Each $m/e=42$ spectrum exhibits a single peak that is an order of magnitude less intense than the largest peak in the $m/e=35$ spectrum at the same scattering angle. The $m/e=35$, $\Theta=10°$ TOF spectra shows four distinct peaks. The slowest of these peaks is attributed to the photodissociation of ClN_3 dimer that could not be completely removed.

In the absence of any secondary dissociation, the Cl and N_3 photofragments will be momentum matched. Under these circumstances, the corresponding TOF spectra should be similar in shape and intensity because the two fragments have similar masses. This expectation is clearly not met, indicating significant spontaneous dissociation of the N_3 frag-

ment. To gain information on the dissociation of N_3 fragments, spectra were taken at $m/e=28(\text{N}_2^+)$ and $14(\text{N}^+)$, samples of which are shown in Fig. 4. There are several possible contributions to these spectra. At 193 nm, the following unimolecular dissociation pathways for N_3 can occur:

$$N_3 \rightarrow N_2(X\ ^1\Sigma_g^+) + N(^4S), \tag{3a}$$

$$N_3 \rightarrow N_2(X\ ^1\Sigma_g^+) + N(^2D), \tag{3b}$$

$$N_3 \rightarrow N_2(X\ ^1\Sigma_g^+) + N(^2P). \tag{3c}$$

In addition, formation of both N_2^+ and N^+ from the dissociative ionization of intact N_3 can occur, as well as N^+ from dissociative ionization of NCl. Owing to substantially more background at $m/e=28$, the $m/e=28$ spectra are considerably noisier than the $m/e=14$ spectra. Analysis of these spectra is considered at length in Sec. IV.

Figure 5 shows TOF spectra taken at different operating conditions. Figures 5(a) and 5(b) show the TOF spectra of $m/e=35$ fragments taken with the laser unpolarized and the parent molecular beam seeded in He and Ne, respectively. Beams seeded in Ne will have slower parent beam velocities than those seeded in He, resulting in slower photofragments, and, thus, better TOF resolution. Figures 5(c) and 5(d) show the TOF spectra of $m/e=35$ fragments taken with the parent molecular beam seeded in Ne and the laser polarized vertically and horizontally, respectively. The relative intensities of the peaks in these spectra are quite different, particularly when comparing the intensities of the fastest two contributions to the spectra. When the laser is vertically polarized, the relative intensity of the middle peak to the fastest is 46%, while that same value for horizontal polarization is 94%. Hence, multiple photofragment angular distributions will be needed to fit the data.

There are significant differences in the TOF spectra for ClN_3 photodissociation at 248 and 193 nm. At 248 nm, the TOF spectra at $m/e=35$ and $m/e=42$ are of comparable intensity, and spectra for both masses show two peaks at several scattering angles. As discussed in the Introduction, these results have been interpreted to indicate the presence of two $\text{Cl}+N_3$ channels: $\text{Cl}+N_3(\text{linear})$ and $\text{Cl}+N_3(\text{HEF})$. In both cases, stable N_3 product is seen, although some of the HEF -N_3 undergoes unimolecular dissociation before reaching the detector. The TOF spectra at 193 nm, in contrast, suggest considerably more dissociation of the N_3 primary product, indicating that much of the additional photon energy is channeled into N_3 internal energy. This effect is quantified in the following section.

IV. ANALYSIS

In this section, we derive center-of-mass translational energy and angular distributions to fit the TOF spectra in Figs. 2–5. By conservation of energy,

$$E_T = h\nu - E_{\text{int}} - D_0, \tag{4}$$

where E_T is the total center-of-mass translational energy, E_{int} is the internal energy of the fragments, and D_0 is the energy difference between the ground states of ClN_3 and the photo-
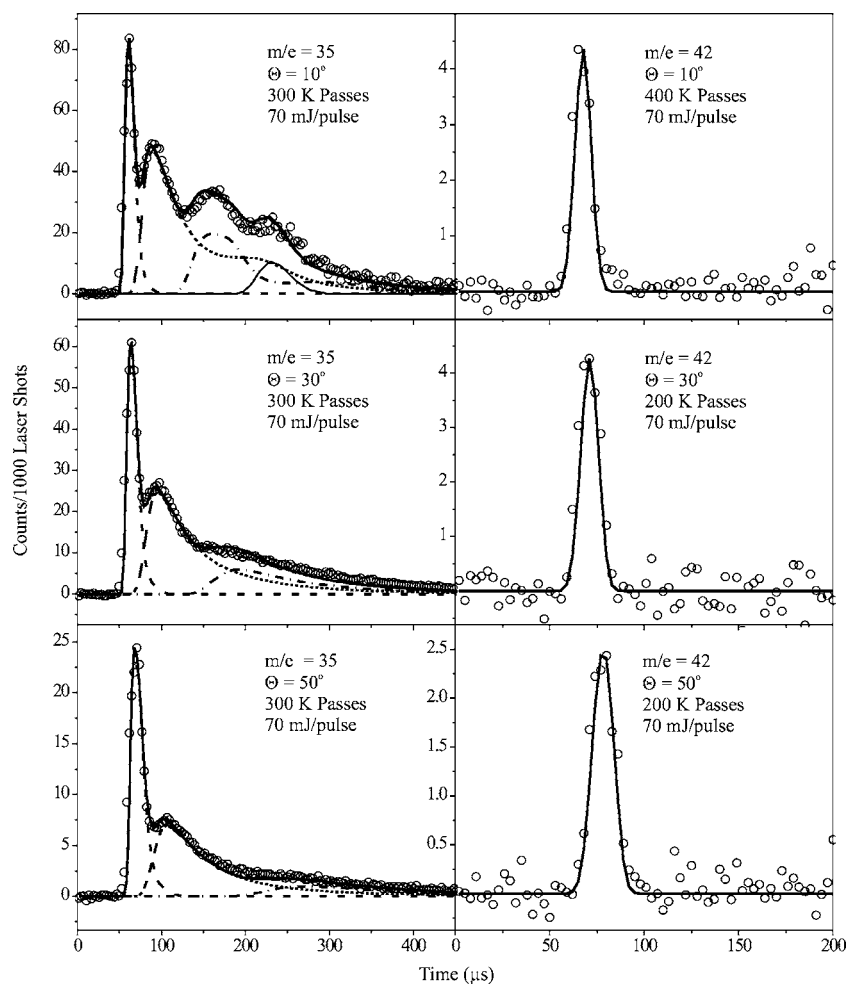
FIG. 3. TOF spectra of $m/e=35$ (Cl$^+$) and $m/e=42$ (N$_3^+$) at detection angles $\Theta=10°$, $30°$, and $50°$ with the parent molecular beam seeded in Ne. For all spectra, the open circles represent the data and the black solid line represents the forward-convolution fit to the data. For the $m/e=35$ data, the dashed lines represent the contributions from the $P(E_T)$ shown in Fig. 6.

fragment channel of interest, assuming no rotational, vibrational, or electronic excitation of the fragments. By determining the translational energy of the fragments, given the energies in Fig. 1, the final photofragment internal energies can be found. Note that Eq. (4) applies not only to two-body dissociation but also events in which secondary dissociation occurs.

Simulations of the observed TOF spectra have been performed using forward-convolution analysis to determine the coupled photofragment energy and angular distribution, $P(E_T, \theta)$, for each channel. For two-body dissociation, this distribution is given by

$$P(E_T, \theta) = P(E_T)I(\theta), \tag{5}$$

where $P(E_T)$ and $I(\theta)$ are the uncoupled center-of-mass translational energy and angular distributions, respectively. The angular distribution is fitted using the following:[21]

$$I(\theta) = \frac{1}{4\pi}(1 + \beta P_2(\cos\theta)). \tag{6}$$

Here, θ is the angle between the photofragment recoil vector and the electric field vector of the dissociation laser, $P_2(\cos\theta)$ is the second Legendre polynomial, and β is an anisotropy parameter characterized by the dissociation event.

The $P(E_T, \theta)$ distribution for each reaction channel is determined by fitting all measured TOFs of two-body dissociation fragments. The TOF spectra for primary dissociation

processes were fitted using the PHOTRAN (Ref. 22) forward-convolution program. This program simulates the TOF spectrum based on "guessed" center-of-mass translational energy $[P(E_T)]$ distributions with a given anisotropy parameter that are iteratively improved until a satisfactory fit to the data is obtained. Beam velocity, laboratory angle, dissociation and ionization volumes, finite angular acceptance angle of the detector, laser power, and polarization angle are additional program parameters used in the forward convolution. This method can be used to simulate the TOF spectrum for Cl fragments even if the N$_3$ counterfragment subsequently dissociates.

A photofragment produced from a primary dissociation event can undergo spontaneous dissociation if its internal energy content from the primary process is sufficiently high. The overall process is then

$$A \xrightarrow{h\nu} B + C \rightarrow B + C_1 + C_2. \tag{7}$$
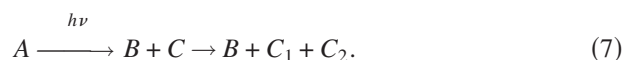
The ANALMAX (Ref. 15) or CMLAB3 (Ref. 23) forward-convolution programs are used to analyze these processes. These programs simulate the TOF spectra much in the same way as previously described. Initially, a fit to the TOF spectrum is generated from a primary center-of-mass translational energy distribution $[P_1(E_{1T})]$, where E_{1T} is the recoil energy of fragments B and C. If photofragment C undergoes unimolecular dissociation, a secondary center-of-mass trans-
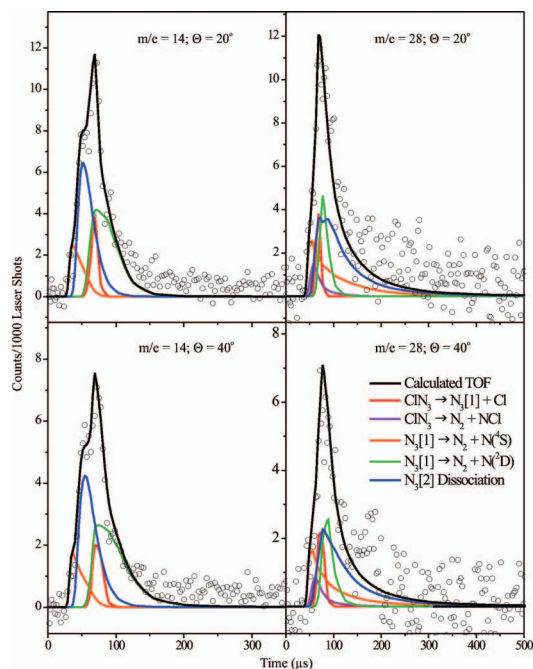
FIG. 4. (Color) TOF spectra of $m/e=14$ (N$^+$) and $m/e=28$ (N$_2^+$) at detection angles $\Theta=20°$ and $40°$ with the parent molecular beam seeded in Ne. For all spectra, the open circles represent the data and the black (solid) line represents the forward-convolution fit to the data. The red line represents the dissociative ionization of detected N$_3$ fragments with the $m/e=42$ $P(E_T)$ shown in Fig. 6. The magenta lines in the $m/e=28$ spectra show the N$_2$ contributions from the molecular elimination channel. The orange and green lines represent secondary dissociation resulting from undetected N$_3$ fragments momentum matched to Cl[1] products, with a secondary $P_2(E_{2T})$ given in Figs. 9(a) and 9(b), respectively. The blue lines represent secondary dissociation resulting from N$_3$ fragments momentum matched to Cl[2] products, with a secondary $P_2(E_{2T})$ given in Fig. 9(c).

lational energy distribution $[P_2(E_{2T})]$ is created for that fragment, where $E_{2T}=\frac{1}{2}\mu_{C_1C_2}v_{\text{rel}}^2$ is the recoil energy of fragments C_1 and C_2 with respect to the center-of-mass of fragment C. One can show that E_T, the center-of-mass recoil energy for all three fragments, is given by

$$E_T = E_{1T} + E_{2T}. \tag{8}$$

The dissociation of fragment C is assumed to be isotropic. Each primary channel can, in principle, result in more than one unimolecular dissociation pathway [i.e., (3a)–(3c)]. For each distinct unimolecular channel, $P_2(E_{2T})$ is assumed to be independent of E_{1T}. $P_1(E_{1T})$ is derived by considering the $P(E_T)$ distribution for fragment B, and the $P_2(E_{2T})$ distributions for all the secondary dissociation channels are varied until the calculated TOF spectra for fragments C_1 and C_2 agree with experiment. The three-body center-of-mass translational energy distribution, $P_3(E_T)$, for a dissociation event in which secondary dissociation occurs is a convolution of $P_1(E_{1T})$ and $P_2(E_{2T})$,

$$P_3(E_T) = \int P_1(E_{1T})P_2(E_T - E_{1T})dE_{1T}. \tag{9}$$

Analysis of the data is organized as follows. First, the radical bond rupture channel is considered because it has been determined to be the dominant channel in the photodissociation. This is performed through analysis of the m/e $=35$ (Cl$^+$) and 42(N$_3^+$) $P(E_T)$ distributions. The molecular elimination channel is then investigated using the m/e $=49$(NCl$^+$) $P(E_T)$ distribution. The $m/e=28$(N$_2^+$) and 14(N$^+$) $P(E_T)$ distributions are examined last because these spectra include contributions from both primary channels and from spontaneous dissociation of the N$_3$ fragment.

A. Radical bond rupture channel: Cl+N$_3$

The $m/e=35$ TOF spectra are fitted using the trimodal $P(E_T)$ distribution given by the solid black line in Fig. 6; the form of this distribution is suggested by the presence of at least three peaks in several of the TOF spectra. The three components of this distribution are labeled Cl[1], Cl[2], and Cl[3], from fastest to slowest. The contribution of each component to the TOF spectra is indicated in Fig. 3. The relative intensities of these three channels are Cl[1]/Cl[2]/Cl[3] $=0.58/0.36/0.06$. The full $P(E_T)$ distribution spans a translational energy range of $0-83$ kcal/mol, while the maximum translational energy release of the ground state Cl+N$_3$ channel is ~99 kcal/mol. Hence, all fragments detected in this dissociation channel have at least 16 kcal/mol internal excitation. By fitting the TOF spectra with different laser polarizations over all measured scattering angles, the anisotropy parameters are found to be $\beta=-0.7$, $\beta=-0.3$, and $\beta=0$ for the Cl[1], Cl[2], and Cl[3] channels, respectively. Figure 7 shows that the Cl[1] and Cl[2] peaks occur at essentially the same translational energies as the two Cl features seen at 248 nm, indicating the additional photon energy at 193 nm is channeled primarily into product internal excitation. In our experiment, we cannot distinguish between Cl($^2P_{3/2}$) and Cl*($^2P_{1/2}$) states, which are separated by 2.3 kcal/mol.

Figure 6 also shows the $P(E_T)$ distribution for the N$_3$ fragment that fits the single peak in the $m/e=42$ TOF spectra of Fig. 3. This distribution is identical to the faster part of the Cl[1] distribution and begins to drop off at $E_T<48$ kcal/mol ($E_{\text{int}}>51$ kcal/mol), falling to zero by $E_T=28$ kcal/mol ($E_{\text{int}}=71$ kcal/mol). The clear implication here is that for primary dissociation events resulting in slower Cl[1] fragments, or any Cl[2] or Cl[3] fragments, the internal energy of the N$_3$ counterfragment is such that it dissociates before reaching the detector. However, the observation that the peak in the TOF distribution for $m/e=42$ is so much weaker than the corresponding TOF feature at m/e $=35$ from the Cl[1] channel implies that even the fastest N$_3$ product is either dissociating prior to reaching the detector or undergoing very efficient dissociative ionization.

In Fig. 6, the right vertical axis represents the maximum translational energy possible for Cl+N$_3$(linear) products (98.5 kcal/mol), and the vertical line marked A at 68.2 kcal/mol indicates the maximum translational energy release of the Cl+N$_3$(cyclic) products, determined using the energetics calculated by Zhang et al.[2] (and shown in Fig. 1). Most of the N$_3$ peak occurs at translational energies that could be associated with linear or cyclic N$_3$, with the exception of the high energy tail that can only be from linear N$_3$, assuming the calculated energetics are correct. The fit to the data is somewhat poorer if this tail is eliminated. The "B" vertical line marked at $E_T=47$ kcal/mol corresponds to the
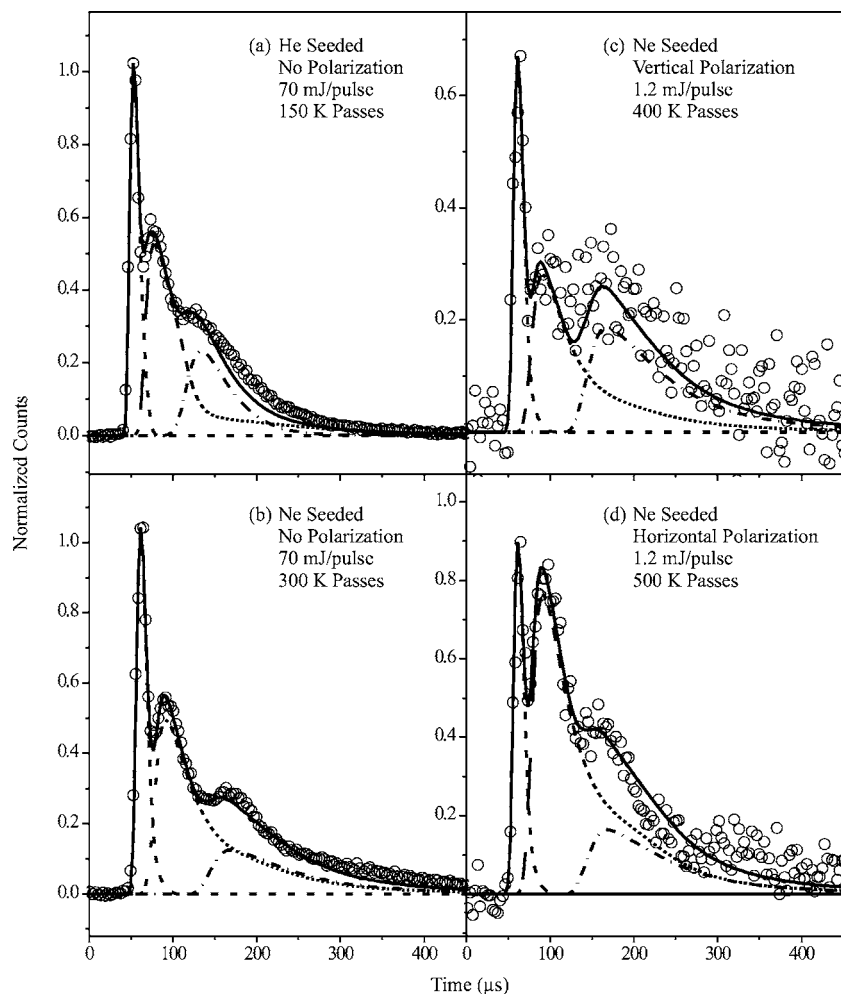
FIG. 5. TOF spectra of $m/e=35$ (Cl$^+$) at detection angle $\Theta=20°$. Figures 5(a) and 5(b) show spectra with the parent ClN$_3$ beam seeded in He and Ne, respectively. Figures 5(c) and 5(d) show spectra taken with the dissociation laser polarized vertically and horizontally, respectively. Spectra in this figure are normalized to both the number of laser shots and the laser power.

calculated minimum (52.47 kcal/mol)[2] in the crossing seam (MSX) for spin-forbidden dissociation of linear N$_3$ to N(^4S)+N$_2$, while the "C" vertical line at 38.9 kcal/mol corresponds to the calculated barrier height (59.64 kcal/mol) for spin-allowed dissociation of linear-N$_3$ to N(^2D)+N$_2$. We note that the loss of N$_3$ signal appears to coincide just after the vertical "B" line, and that no signal is seen for N$_3$ internal energies above the barrier for spin-allowed dissociation. The implications of these observations are discussed in more detail below.

B. Molecular elimination channel: NCl+N$_2$

The $P(E_T)$ distribution for NCl+N$_2$ at 193 nm, shown in Fig. 8, comprises a single feature with average translational energy $\langle E_T \rangle = 30.6$ kcal/mol. The distribution falls to zero well before the maximum translational energy release allowed for production for N$_2(X\,^1\Sigma_g^+)$ and any of the three low-lying NCl states (i.e., $X\,^3\Sigma^-$, $a\,^1\Delta$, and $b\,^1\Sigma^+$, see Fig. 1). Hence, the $P(E_T)$ distribution does not provide much information on the state distribution of the NCl, although previous studies have shown that NCl($a\,^1\Delta$) is the dominant NCl product channel from UV photolysis of ClN$_3$.[1,7,9] Note that $\langle E_T \rangle$ at 193 nm is similar to the value seen at 248 nm, $\langle E_T \rangle = 28.4$ kcal/mol,[5] indicating that the additional photon energy is channeled into product internal excitation, similar to what was seen for channel (2).

C. N$_2$ and N fragments

The discussion in Sec. IV A indicates that there is a significant dissociation of the N$_3$ photoproduct prior to detection owing to its high degree of internal excitation. Unimolecular dissociation of N$_3$ can be investigated more directly through analysis of the TOF spectra at $m/e=14$ and 28, corresponding to N$^+$ and N$_2^+$ ions. The $P(E_T)$ distribution for $m/e=35$ products implies that N$_3$ is produced with three ranges of internal energy, N$_3$[1–3], corresponding to Cl[1–3] products. All the N$_3$[2] and N$_3$[3] dissociate before reaching the detector, as does a significant fraction of the N$_3$[1]. Moreover, each N$_3$ population can undergo dissociation to at least two channels, namely, spin-forbidden dissociation to N(^4S)+N$_2$ and spin-allowed dissociation to N(^2D)+N$_2$. There is also a contribution to both masses from dissociative ionization of any N$_3$[1] that survives in transit to the detector. Given the large number of possible contributions to the signal at these ion masses, we have fitted the data using as few channels as possible and making physically reasonable assumptions about the energetics of the contributing secondary dissociation processes. The resulting fits are probably not unique but show which secondary processes are consistent with our data.

We begin by noting that the central peak in the two $m/e=14$ spectra in Fig. 4, when corrected for differences in flight time through the quadrupole mass spectrometer,
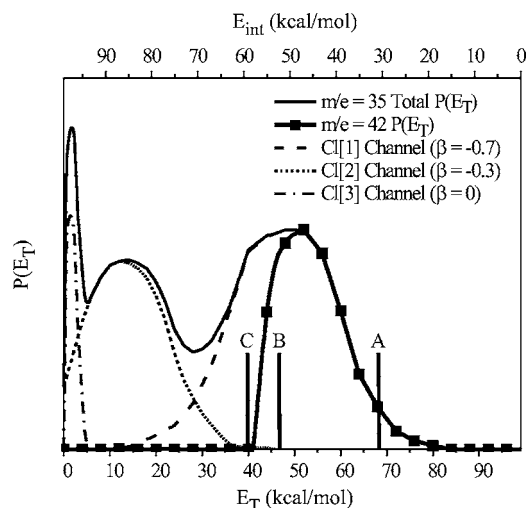
FIG. 6. Center-of-mass translational energy distribution ($P(E_T)$) for radical bond rupture channel forming Cl and N_3 in the ClN_3 photodissociation. The dashed lines correspond to the three different contributions to the $m/e=35$ spectra. Their sum is represented by the black line and was used to fit the total $m/e=35$ spectra in Fig. 3. The solid black line with squares shows the $P(E_T)$ used to fit the $m/e=42$ spectra in Fig. 3. The bottom axis shows the translational energy release of detected fragments, and the top axis shows the corresponding internal energy of the fragments. The right axis represents the maximum translational energy for $Cl+N_3$(linear) and the vertical line marked "A" shows the theoretical maximum translational energy release[2] for $Cl+N_3$(cyclic), $E_T=68.8$ kcal/mol. Vertical line B shows the position where the intersystem crossing to the quartet state leading to spin-forbidden products occurs ($E_T=45.6$ kcal/mol). Vertical line C shows the maximum translational energy necessary for formation of the linear-N_3 transition state to spin-allowed products ($E_T=39.4$ kcal/mol) (Ref. 2).

matches the single N_3 peak in the $m/e=42$ spectra. This contribution is shown as the red line in Fig. 4 and represents dissociative ionization (DI) of detected $N_3[1]$ fragments. There is clearly signal at faster and slower arrival times than the DI signal. The faster signal is assigned to unimolecular dissociation of the undetected $N_3[1]$ fragments, as these are the fastest N_3 fragments and their dissociation will lead to even faster N and N_2 in the laboratory frame.

Comparison of the $N_3[1]$ and $Cl[1]$ $P(E_T)$ distributions in Fig. 6 shows that the two distributions track one another from high E_T down to $E_T \cong 51$ kcal/mol, below which the N_3 distribution drops off, and that no $N_3[1]$ signal is seen for $E_T < 40$ kcal/mol. As mentioned above, this cutoff value corresponds to the calculated barrier height, 59.6 kcal/mol, for spin-allowed dissociation to $N(^2D)+N_2$. Hence, we assume that the faster undetected $N_3[1]$ fragments, produced with internal energies between the inter-system crossing (ISC)

minimum energy and the spin-allowed barrier, dissociate to $N(^4S)+N_2$, while the slower undetected $N_3[1]$ has undergone dissociation to $N(^2D)+N_2$. The resulting $P_2(E_{2T})$ distributions and total $P_3(E_T)$ distributions [Eq. (9)] from both contributions are shown in Figs. 9(a) and 9(b), and the simulated contributions to the TOF spectra at $m/e=14$ and 28 are shown as orange and green lines in Fig. 4.

The remaining feature in the $m/e=14$ TOF spectra was fitted using the $P_2(E_{2T})$ distribution shown in Fig. 9(c). This distribution simulates the dissociation of the $N_3[2]$ fragments. The overall $P_3(E_T)$ distribution predominantly spans the energy range expected for $N_2(X\,^1\Sigma_g^+)+N(^2D)$ products. However, this distribution extends beyond the maximum translational energy release of reaction (3b), indicating some dissociation to $N_2+N(^4S)$, as well. The contribution to the TOF data from these products is shown as the green line in Fig. 4.

The combination of DI and the three unimolecular dissociation processes discussed above is sufficient to fit the $m/e=14$ data, so no further contributions were considered, such as dissociative ionization of N_2 or NCl from channel (1). For the $m/e=28$ data, direct ionization of the N_2 product from channel (1) was included and shown as the magenta line. In our previous work at 248 nm,[5] a contribution to the N and N_2 TOF data was included from N_3 secondary photodissociation from absorption of an additional photon. Such a contribution was not needed here, possibly reflecting the fact that most N_3 produced at 193 nm undergoes spontaneous dissociation before it can absorb a second photon.

V. DISCUSSION

Interpretation of our results for ClN_3 photodissociation at 193 nm is facilitated by comparison with previous work at 248 nm.[5,15] At both wavelengths, $NCl+N_2$ is a minor channel, so we focus mainly on $Cl+N_3$ products. Figure 7 compares the $P(E_T)$ distributions used to fit the Cl fragments at 193 and 248 nm. At 248 nm, two peaks were seen, with the faster peak assigned to $Cl+N_3$(linear) products and the slower to $Cl+N_3$(HEF) products. It is quite striking that the translational energies for these two peaks at 248 nm line up with the $Cl[1]$ and $Cl[2]$ peaks at 193 nm, implying that the additional 1.4 eV of available energy at 193 nm is channeled very efficiently into N_3 internal energy. This result is somewhat unexpected for a small molecule, where one would generally expect at least some partitioning of the additional photon energy into translational energy of the
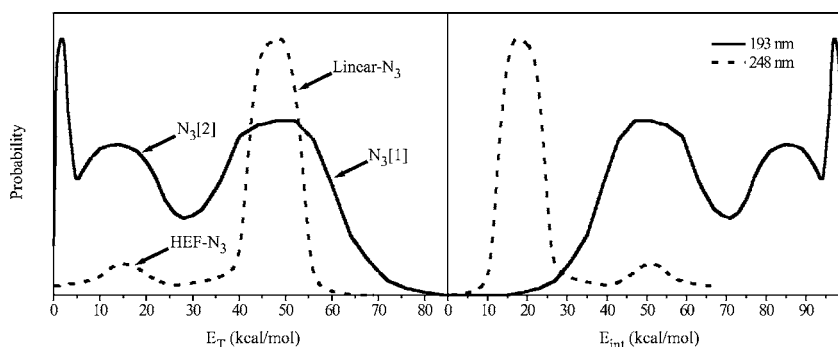

FIG. 7. Left: comparison of $m/e=35$ $P(E_T)$ distributions of 248 and 193 nm photodissociation. Right: same comparison plotted vs N_3 internal energy E_{int}.
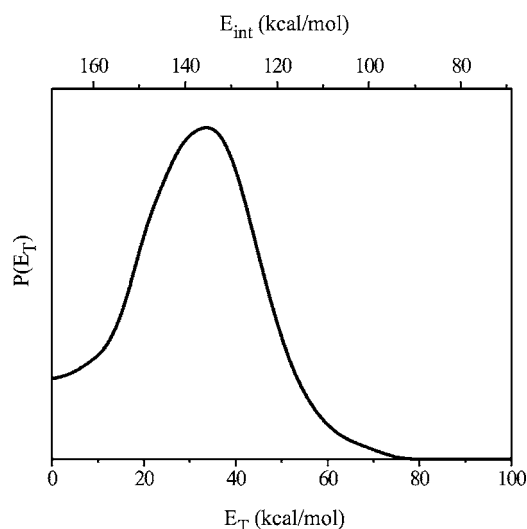
FIG. 8. Center-of-mass translational energy distribution ($P(E_T)$) for NCl $+N_2$ products. The bottom axis shows the translational energy release of detected fragments, and the top axis shows the corresponding internal energy of the fragments from the ground states of NCl+N_2.

photofragments.[24] It implies that we are not, for example, simply accessing a directly repulsive electronic state correlating to ground state Cl+N_3 products, but instead are observing the results of a more complex dissociation mechanism in which the excess energy relative to 248 nm appears as additional N_3 excitation. In this section, we consider the dissociation mechanism at 193 nm based on the $P(E_T)$ distributions, the anisotropy parameters, and the previous results at 248 nm.

At 248 nm, we found anisotropy parameters $\beta=1.7$ and 0.4 for Cl+N_3(linear) and Cl+N_3(HEF) dissociation chan-

nels, respectively,[5] whereas at 193 nm, $\beta=-0.7$ for Cl[1] and -0.3 for Cl[2]. Hence, at both wavelengths, the faster Cl peak is associated with a more anisotropic photofragment angular distribution than the slower peak, but the sign of the anisotropy has changed, with fragments preferentially recoiling perpendicular to the laser polarization at 193 nm and parallel at 248 nm. At 248 nm, one accesses the $\widetilde{B} \, ^1A'(S_2)$ excited state from the $\widetilde{X} \, ^1A'(S_0)$ ground state, a parallel transition, while absorption at 193 nm lies within a band assigned to a perpendicular transition to the $\widetilde{C} \, ^1A''(S_3)$ state;[11] this state ordering is the same as that proposed for HN$_3$.[25] Our photofragment angular distributions are consistent with these assignments and show that at both wavelengths, the initial molecular orientation is imprinted on the fastest photofragments, but that the slower channel exhibits significantly more orientational scrambling.

The similar peak splitting between the Cl[1] and Cl[2] channels at 193 nm and the Cl+N_3(linear) and Cl $+N_3$(HEF) channels at 248 nm implies that the Cl[1] and Cl[2] channels at 193 nm correspond to similar final states as at 248 nm, namely Cl+N_3(linear) and Cl+N_3(HEF). With this assignment, essentially all of the additional photon energy at 193 nm is directed into internal energy of the N_3 for both channels. The implication of this assignment is that all detected N_3 fragments correspond to linear N_3. The high energy form observed during 248 nm dissociation is still produced during 193 nm dissociation, but its large amount of internal energy results in dissociation before detection.

One can gain additional insight into the photodissociation dynamics of ClN$_3$ through consideration of the more thoroughly studied HN$_3$ molecule.[25,26] In particular, recent theoretical and experiment work on the photodissociation of
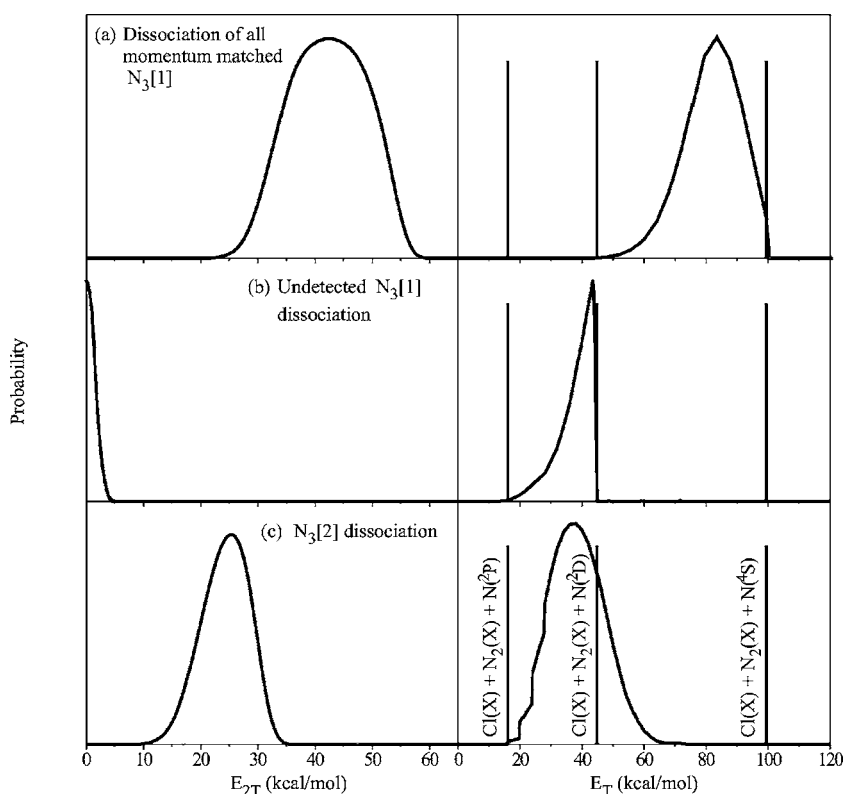

FIG. 9. Center-of-mass translational energy distributions modeling the secondary dissociation of N_3 molecules produced from ClN$_3$ photodissociation. The black distributions are used to simulate the observed spectra in Fig. 4 where their contributions can be seen as the orange (9a), green (9b), and blue (9c) lines in that figure. The distributions to the right are the total $P_3(E_T)$ calculated using Eq. (9) using a $P_2(E_{2T})$ equal to the black line. The vertical lines show the maximum translational energy release for the reaction channel listed.
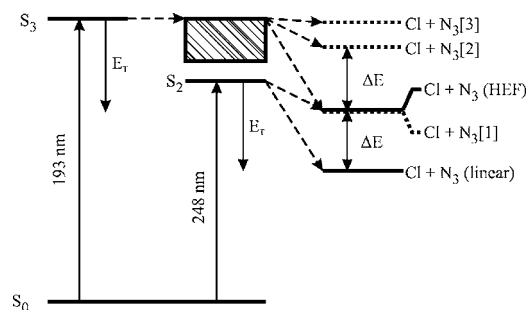
FIG. 10. Schematic depiction of ClN_3 dissociation at 193 and 248 nm. Dissociation at both wavelengths results in similar values of E_T and ΔE [peak splittings in $P(E_T)$ distributions]. The $Cl+N_3(HEF)$ and $Cl+N_3[1]$ dissociation channels are produced with nearly identical internal energies (which can easily be seen in Fig. 7).

HN_3 has shown evidence for two $H+N_3$ decay channels that were assigned to parallel decay pathways on the S_1 surface.[27] The fast channel, with $\beta \cong -0.8$, was attributed to excitation of the perpendicular $S_0(\widetilde{X}\,^1A') \rightarrow S_1(\widetilde{A}\,^1A'')$ transition followed by rapid N–H bond dissociation. The slower channel, favored at higher photon energies and for which $\beta \cong 0$, was assigned to $S_2 \rightarrow S_1$ internal conversion via a conical intersection followed by isomerization through a cyclic, slightly nonplanar transition state on the S_1 surface. The more complex dynamics associated with the latter mechanism is presumably reflected in the more isotropic photofragment angular distribution, regardless of whether the N_3 product is cyclic.

Similar mechanisms may well be operative for ClN_3; the faster channel is more direct and anisotropic at both wavelengths, while the anisotropy of the Cl[2] channel is reduced because it results from isomerization through a tight transition state. However, while the two HN_3 channels appear to result from excitation of the overlapping transitions to the S_1 and S_2 states, only the S_2 state of ClN_3 is accessible at 248 nm. One therefore cannot say if the dynamics that produce branching between the two N_3 channels occur on the S_2 or S_1 states until these excited states are better characterized. At 193 nm, a different electronic state is initially excited, but the observation that the additional photon energy is partitioned almost entirely into N_3 internal energy for the Cl[1] and Cl[2] channels suggests that the mechanism for bifurcation between the two channels is the same as at 248 nm.

These considerations suggest the overall mechanism depicted in Fig. 10 for ClN_3 photodissociation at 193 nm, in which excitation to the S_3 state is followed by $S_3 \rightarrow S_2$ internal conversion, with production of the Cl[1] and Cl[2] channels resulting from dynamics on either the S_2 or S_1 surface. The additional energy relative to 248 nm is channeled into internal energy as these internal conversion steps occur, ultimately appearing in the N_3 products. Overall, the similarities in the dynamics at the two wavelengths support significant commonality in the dissociation mechanisms. We point out, however, that the branching between Cl[1] and Cl[2] is quite different at the two wavelengths, with considerable enhancement of Cl[2] at 193 nm, and a global photodissociation mechanism must ultimately account for this effect.

There is an alternate interpretation of the data at 193 nm

based on another remarkable but less obvious correspondence between the data at the two wavelengths. At 193 nm, the internal energy E_{int} corresponding to the maximum of the Cl[1] distribution is 50 kcal/mol, in excellent agreement with $E_{int}=51$ kcal/mol for the maximum of the Cl $+N_3(HEF)$ peak at 248 nm. This correspondence can easily be seen in the comparison of the internal energy distributions shown in the right panel of Fig. 7. One could therefore interpret the 193 nm data by assigning the Cl[1] distribution to $Cl+N_3(HEF)$ rather than $Cl+N_3(linear)$. This interpretation implies that $Cl+N_3(linear)$ products are not produced at 193 nm, and that all of the detected N_3 fragments (see Fig. 6) are HEF-N_3.

If HEF-N_3 does have a cyclic structure, the fact that the additional 32.8 kcal/mol photolysis energy is dispensed internally to the N_3 fragment is consistent with the theoretical 30.3 kcal/mol cyclization energy for N_3.[2] With this assignment, the coincidental similarity between the cyclization energy and the additional photon energy explains why the radical bond rupture fragments are produced with the same translational energies at both wavelengths. Note that most of these N_3 fragments lie within the calculated range of energies allowed for cyclic N_3; the maximum E_{int} of detected N_3 fragments is 58.1 kcal/mol, a value close to the calculated barrier height of 63.38 kcal/mol for dissociation of cyclic N_3 to $N(^2D)+N_2$ products, while only the fastest $Cl+N_3$ products lie beyond the maximum E_T of 68.2 kcal/mol for Cl $+N_3(cyclic)$ fragments. This maximum was determined using $D_0(Cl-N_3)=49.6$ kcal/mol, a value consistent with both the VMI experiments[4] (which provide an upper bound to D_0) and MP2 calculations of the bond energy.[28] Recent unpublished work, however, has suggested a considerably lower bond energy of 42.9 kcal/mol.[29] If this lower bond energy is correct, the maximum E_T for the $Cl+N_3(cyclic)$ fragments would be 74.9 kcal/mol, placing even more of the detected N_3 fragments within the bounds for cyclic N_3. In any case, this alternate assignment is attractive from the perspective of establishing cyclic N_3 as a stable photoproduct at 193 nm. It is also consistent with the interpretation of recent work on ClN_3 photodissociation at 157 nm.[30]

However, the alternate assignment suffers from several shortcomings. First, the high degree of anisotropy observed for the Cl[1] channel is inconsistent with the extent of nuclear rearrangement required for the production of cyclic N_3. Secondly, this assignment offers no explanation for the presence of the Cl[2] channel and why the Cl[1]–Cl[2] splitting at 193 nm is so similar to that between the Cl $+N_3(linear)$ and $Cl+N_3(HEF)$ channels at 248 nm. Finally, the energetics for the $N_3[1]$ signal are in better agreement with the calculations of Zhang et al.[2] on ISC crossings and dissociation transition states for linear N_3 than for cyclic N_3. For example, with a Cl–N bond energy of 49.6 kcal/mol, if the $N_3[1]$ signal were from cyclic N_3, then it should start to drop off at $E_T=40$ kcal/mol from spin-forbidden dissociation, and disappear for $E_T<36$ kcal/mol. These two values are in poorer agreement with the results in Fig. 6 than the corresponding values assuming linear N_3. We thus believe the correspondence between the two wavelengths given in the preceding paragraphs to be more plausible. Our preferred

interpretation is supported indirectly by the molecular elimination channel 1, for which the additional photon energy at 193 nm relative to 248 nm is also directed almost entirely into product internal energy.

We close by considering the relatively minor Cl[3] channel. This channel corresponds to very high internal N_3 internal energies, in the range of 95–100 kcal/mol. We can rule out production of $Cl+N_3(\widetilde{A}\,^2\Sigma_u^+)$ as the origin of this channel, as the $N_3(\widetilde{A}\,^2\Sigma_u^+)$ state is out of range at 193 nm (see Fig. 1).[31] The isotropic angular distribution and low translational energy release for Cl[3] could result from internal conversion to the ground state followed by statistical decay. The corresponding N_3 fragment will then have sufficient energy to dissociate to $N_2+N(^4S)$, $N(^2D)$, or $N(^2P)$.

VI. CONCLUSIONS

The photodissociation of ClN_3 at 193 nm has been investigated and compared to previous work at 248 nm. We find that the $Cl+N_3$ channel strongly dominates over $NCl+N_2$, just as at 248 nm. The $P(E_T)$ distribution for the Cl atoms is trimodal, and the photofragment angular distributions for the two fastest channels are consistent with a perpendicular excitation to the $\widetilde{C}\,^1A''$ of ClN_3, as opposed to the $\widetilde{B}\,^1A'$ state accessed at 248 nm. A key result of this paper is that essentially all the additional photon energy at 193 nm vs 248 nm is partitioned into product internal energies for both channels. As a result, most of the N_3 product is formed with sufficient internal energy to undergo unimolecular decay to $N+N_2$ channels, and we observe evidence for spin-forbidden and spin-allowed dissociations to $N(^4S)$ and $N(^2D)$, respectively.

The fastest two peaks in the $P(E_T)$ distributions for the Cl products (the Cl[1] and Cl[2] peaks) at 193 nm have very similar translational energies as the two peaks seen at 248 nm. These were previously assigned to $Cl+N_3$(linear) and $Cl+N_3$(HEF), with the HEF-N_3 showing energetics consistent with cyclic N_3. This correspondence, along with comparison of the photofragment angular distributions, suggests that the same assignment be made at 193 nm, and that the same bifurcation of the dynamics at 248 nm responsible for two N_3 channels is operative at 193 nm. However, at 193 nm, only the fastest N_3 product associated with the Cl[1] channel is detected. The slower linear N_3 and all the HEF-N_3 dissociate prior to detection. Hence, even if the HEF-N_3 produced at 193 nm is cyclic, it is produced with too much internal energy to survive on the time scale of our experiment.

[1] N. Hansen, A. M. Wodtke, A. V. Komissarov, and M. C. Heaven, Chem. Phys. Lett. **368**, 568 (2003).
[2] P. Zhang, K. Morokuma, and A. M. Wodtke, J. Chem. Phys. **122**, 014106 (2004).
[3] A. J. Ray and R. D. Coombe, J. Phys. Chem. **99**, 7849 (1995); T. L. Henshaw, G. C. Manke II, T. J. Madden, M. R. Berman, and G. D. Hager, Chem. Phys. Lett. **325**, 537 (2000).
[4] N. Hansen and A. M. Wodtke, J. Phys. Chem. A **107**, 10608 (2003).
[5] N. Hansen, A. M. Wodtke, S. J. Goncher, J. C. Robinson, N. E. Sveum, and D. M. Neumark, J. Chem. Phys. **123**, 104305 (2006).
[6] K. Dehnicke and P. Ruschke, Z. Naturforsch. B **33**, 750 (1978); T. C. Clark and M. A. A. Clyne, Trans. Faraday Soc. **65**, 2994 (1969).
[7] R. D. Coombe, D. Patel, A. T. Pritt, Jr., and F. J. Wodarczyk, J. Chem. Phys. **75**, 2177 (1981).
[8] R. D. Coombe, S. J. David, T. L. Henshaw, and D. J. May, Chem. Phys. Lett. **120**, 433 (1985); N. Hansen, A. M. Wodtke, A. V. Komissarov, K. Morokuma, and M. C. Heaven, J. Chem. Phys. **118**, 10485 (2003).
[9] A. V. Komissarov, G. C. MankeII, S. J. Davis, and M. C. Heaven, J. Phys. Chem. A **106**, 8427 (2002).
[10] T. L. Henshaw, S. D. Herrera, G. W. Haggquist, and L. A. V. Schlie, J. Phys. Chem. A **101**, 4048 (1997).
[11] K. Morokuma (private communication).
[12] P. Samartzis, N. Hansen, and A. Wodtke, Phys. Chem. Chem. Phys. **8**, 2958 (2006).
[13] M. Bittererova, H. Ostmark, and T. Brinck, J. Chem. Phys. **116**, 9740 (2002).
[14] D. Babikov, P. Zhang, and K. Morokuma, J. Chem. Phys. **121**, 6743 (2004); D. Babikov, B. K. Kendrick, P. Zhang, and K. Morokuma, *ibid.* **122**, 044315 (2005).
[15] A. M. Wodtke, ANALMAX (2004).
[16] R. H. Jensen, A. Mann, and R. D. Coombe, J. Phys. Chem. A **104**, 6573 (2000).
[17] P. C. Samartzis, J. J.-M. Lin, T.-T. Ching, C. Chaudhuri, Y. T. Lee, S.-H. Lee, and A. M. Wodtke, J. Chem. Phys. **123**, 051101 (2005).
[18] Y. T. Lee, J. D. McDonald, P. R. LeBreton, and D. R. Herschbach, Rev. Sci. Instrum. **40**, 1402 (1969).
[19] J. C. Robinson, S. A. Harris, W. Sun, N. E. Sveum, and D. M. Neumark, J. Am. Chem. Soc. **124**, 10211 (2001).
[20] D. Proch and T. Trickl, Rev. Sci. Instrum. **60**, 713 (1989).
[21] G. E. Busch and K. R. Wilson, J. Chem. Phys. **56**, 3638 (1972); R. N. Zare, Mol. Photochem. **4**, 1 (1972).
[22] S. A. Harich, PHOTRAN (2003).
[23] S. A. Harich, CMLAB3 (1989).
[24] R. Schinke, *Photodissociation Dynamics* (Cambridge University Press, Cambridge, 1993).
[25] J. Zhang, K. Xu, and G. Amaral, Chem. Phys. Lett. **299**, 285 (1999).
[26] M. Lock, K. H. Gericke, and F. J. Comes, Chem. Phys. **213**, 385 (1996); R. L. Cook and M. C. L. Gerry, J. Chem. Phys. **53**, 2525 (1970).
[27] J. Zhang, P. Zhang, Y. Chen, K. Yuan, S. A. Harich, X. Wang, Z. Wang, X. Yang, K. Morokuma, and A. M. Wodtke, Phys. Chem. Chem. Phys. **8**, 1690 (2006).
[28] M. Otto, S. D. Lotz, and G. Frenking, Inorg. Chem. **31**, 3647 (1992).
[29] A. Quinto-Hernandez, Y.-Y. Lee, T.-P. Huang, W.-C. Pan, J. J. Lin, P. Bobadova-Paranova, K. Morokuma, P. C. Samartzis, and A. M. Wodtke, Int. J. Mass. Spec. (submitted).
[30] P. C. Samartzis, J. J. Lin, T.-T. Ching, C. Chaudhuri, Y. T. Lee, S.-H. Lee, and A. M. Wodtke, J. Chem. Phys. (submitted).
[31] A. E. Douglas and W. J. Jones, Can. J. Phys. **43**, 2216 (1965); R. E. Continetti, D. R. Cyr, D. L. Osborn, D. J. Leahy, and D. M. Neumark, J. Chem. Phys. **99**, 2616 (1993).